Application of the empirical line method (ELM) to calibrate the airborne Daedalus-CZCS scanner

Loredana Pompilio, Lucia Marinangeli, Luigi Amitrano, Giacomo Pacci, Salvatore D'andrea, Salvatore Iacullo & Enrico Monaco

Published online: 26 Nov 2017.

Submit your article to this journal ☑

View related articles ☑

View Crossmark data ☑

Taylor & Francis
Taylor & Francis Group

 OPEN ACCESS   Check for updates

Application of the empirical line method (ELM) to calibrate the airborne Daedalus-CZCS scanner

Loredana Pompilio [a], Lucia Marinangeli[a], Luigi Amitrano[b], Giacomo Pacci[b], Salvatore D'andrea[b], Salvatore Iacullo[b] and Enrico Monaco[b]

[a]Dipartimento di Scienze Psicologiche, Università G. D'Annunzio, Chieti Scalo, Italy; [b]III Nucleo Aereo Guardia Costiera Pescara, Servizio Telerilevamento Ambientale, Pescara, Italy

ABSTRACT

The present investigation aims at providing a reliable evaluation of the geometric and radiometric accuracy of the airborne Daedalus-Coastal Zone Color Scanner (CZCS), through cal/val techniques. To this aim, on November 2014, we accomplished a remote sensing campaign over the Peligna Valley (Italy). Together with the personnel of the III Nucleo Aereo of the Italian Coast Guard, based at the Pescara Airport, we deployed the Daedalus AA1268EM1 CZCS scanner on board the fixed-wing aircraft type ATR42MP and a ASD FieldSpec spectroradiometer for a simultaneous field survey. We used vicarious calibration and secondary non-parametric geometric correction to achieve absolute atmospheric correction and geometric calibration, respectively. Although the validation and calibration targets used in this study were similar in nature, correlation coefficients of the prediction equations between at-sensor radiance and ground reflectance were > 0.90 for each of the 10 CZCS wavebands and the independent error assessment demonstrate that the empirical line method can be applied to correct CZCS imagery with satisfactory results.

Introduction

Beside the many scientific purposes, remote sensing techniques are widely used with the aim of promoting far-sighted policies for the management and sustainability of our societies. As a consequence, the requirement of quantitative datasets is mandatory. To provide the optical remotely sensed data with quantitative value, it is necessary to calibrate them both geometrically and radiometrically (Smith & Milton, 1999) and accomplish an absolute atmospheric correction (Clark, Suomalainen, & Pellikka, 2011a). Therefore, remote sensing calibration and validation (cal/val) are critical aspects of Earth observation measurements that have to be accomplished for the correct exploitation of the dataset (Teillet et al., 2001).

Calibration allows to retrieve the relationship between ground-based position and radiance and the image-based coordinates and brightness, respectively. Validation of the results allows to assess the accuracy of the calibration process and thus the level of confidence in the interpretation of the derived products. As a consequence, calibrated and validated remote measurements will not be biased by atmospheric conditions, illumination and reflection geometry, sensor characteristics, platform stability and data processing effects.

Different studies based on the data acquired with the airborne Daedalus CZCS (Coastal Zone Color

Scanner; DaedalusScanners Imaging Systems and Services) and its paired Advanced Thematic Mapper scanners appeared in the literature (Zambianchi et al., 1990; Shennan & Donoghue, 1992; Meinel, Netzband, Amann, Statter, & Kritikos, 1996; Roy, Devereux, Grainger, & White, 1997; Kiema & Bahr, 2001; Rowlands & Sarris, 2007; Challis, Kincey, & Howard, 2009; and references therein) to show the fruitful data exploitation for applications such as detection of archaeological remains, urban environment classification and geological prospection. This study focuses on the accuracy assessment of CZCS data calibration as a preliminary and mandatory requirement before other processing steps focusing in research applications.

The advent of high performance integrated global positioning/inertial systems (GPS/INS) allows the direct georeferencing of airborne sensors to become feasible (Cramer & Stallmann, 2002). Direct georeferencing uses parametric approaches to correct for the geometric distortions inherent in remotely sensed images, due to platform instability and sensor-dependent distortions (Roy et al., 1997). Direct georeferencing of CZCS flight lines is accomplished through the geocorrection software utility provided by the manufacturer. In order to remove the geometric distortions affecting airborne imagery, information concerning

CONTACT Loredana Pompilio ✉ loredana.pompilio@unich.it 🏛 Università G. D'Annunzio, Dipartimento di Scienze, della Salute e del Territorio, Via dei Vestini, 32, Chieti Scalo, Italy

the sensing geometry, sensor external orientation parameters and the relief are required. Attitude and position of the sensor at the time of acquisition is recorded with the GPS/INS subsystem on-board the aircraft and provided to the geocoding routine. A Digital Elevation Model (DEM) with proper resolution is provided by the operator, as well. In the absence of proper elevation data or in case of flat terrain, the software tool can provide a temporary elevation dataset representing a flat Earth model to be used in place of the DEM. The whole geocoding routine is completely automatic with scarce control of the operator. In addition, several uncertainties may derive from biases in the inertial measurement unit, placement of it relative to the sensor optical axis or other causes.

To be aware of the amount of uncertainties occurring in the semi-automatic geocoding process of CZCS flight lines, we accomplished an accuracy assessment through the co-registration of our dataset with high resolution orthophotos available over the same region. This is an indirect method for having an understanding of the geometric accuracy of the dataset in that it relies on a posteriori analysis and independent datasets (Honkavaara et al., 2006; Moniwa, 1980).

To deal with remotely sensed data of quantitative value, radiometric calibration is also required. Especially optical data are affected by sensor characteristics, illumination geometry and atmospheric conditions. Optical sensor calibration is achieved using known gain and offset coefficients to convert digital numbers (DNs) into at-sensor radiance (L_{SS}; W m^{-2} sr^{-1} μm^{-1}). Through normalising for variations due to Earth-Sun distance and Solar Zenith angle it is also possible to convert the at-sensor radiance into at-sensor reflectance (ρ_{SS}). At this point, the contribution of the atmosphere and the effects of an off-nadir view are still present (Clark et al., 2011a).

Several methods account for the effects of illumination and the atmosphere on at-sensor radiance, including (a) normalisation to a spectrally flat target or an image average; (b) radiative transfer models simulating the interaction between radiation and both the atmosphere and the surface; and (c) empirical relationships between at-sensor radiance and ground reflectance. The performance of these different methods have been compared by a number of authors (Farrand, Singer, & Merényi, 1994; Ben-Dor, Kindel, & Goetz, 2004; Gao, Montes, Davis, & Goetz, 2009; Brook & Ben-Dor, 2011; and references therein).

In the present work, we use vicarious calibration methods to achieve absolute atmospheric correction by empirically evaluating the relationship between at-sensor radiance (L_{SS}) and field measurements of surface reflectance (ρ_s), assuming this relationship is linear (Clark, Suomalainen, & Pellikka, 2011b). Therefore we acquire reflectance measurements of ground targets during (or close in time to) the sensor overpass, thus to represent the spectral variability collected from remote and to ensure a wide dynamic range of albedo to be covered. Then we calibrate the at-sensor radiance to reflectance via the empirical line method (ELM).

In summary, in this study, we evaluate the CZCS (model Daedalus AA1268EM1 on-board of the aircraft ATR42MP) data quality through field *cal/val* operations. Therefore, the aim of the present work is twofold: (a) to assess both the geometric and radiometric accuracy of the Daedalus CZCS scanner observations; (b) to determine to what extent this instrument may assist in landscape observations and quantitative applications. We describe instruments used and methods applied in this study in "Methods" section and present results and discussion in "Results and discussion" section.

Methods

To evaluate the geometric accuracy and retrieve surface reflectance from airborne data, we accomplished a remote sensing campaign in 2014 (Table 1).

In its standard configuration, the Daedalus 1268 CZCS sensor is provided with 10 spectral channels, spanning the wavelength interval between the visible (VIS) and short wave infrared (SWIR), and an additional thermal infrared channel, acquired in both high and low gain. The spectral characteristics of the AA1268EM1 CZCS sensor are listed in Table 2. The surface brightness is digitised into 12-bit grey level values and converted into units of radiance using in-flight calibration files. The sensor IFOV (Instantaneous Field Of View) is 2.5 mrad and the optical field of view (FOV) is 86° (Table 2). Scan rate, swath width and ground pixel size vary according to the flight height and velocity of the overhead platform. A GPS/INS subsystem is also provided for measurements of location and scan head attitude in the three axes.

Table 1. Characteristics of the 2014 remote sensing campaign.

	2014 Campaign
Date	10 November 2014
Time (UTC)	11:00
Average Height (m a.g.l.)	700
Spatial resolution (m/pixel)	1.5
Spectral resolution	10 ch. in 0.4–2.25 μm
Scan rate (Hz)	100
IFOV (mrad)	2.5
FOV (deg)	86
Wind Speed (kn)	2
Wind Direction	Variable
Sun Azimuth (deg)	166.68
Sun Elevation (deg)	29.67

ch: channel.

Table 2. AA1268EM1 CZCS sensor bandsets (nm).

Band	Centre	Width	Start	End
1	443	20	430	450
2	490	20	480	500
3	520	30	500	530
4	560	30	540	570
5	605	50	580	630
6	670	70	630	700
7	765	100	710	810
8	885	110	830	940
9	1650	200	1550	1750
10	2200	270	2080	2350
11	11,000	4500	8500	14,000

Remote sensing campaign

We selected the Northern most sector of the Peligna Valley as test field for geometric and surface reflectance calibration, respectively. The Peligna Valley lies in the central part of the Abruzzo region of Italy (Figure 1). Topography is flat inside the valley with average elevation of 350 m a.s.l., rapidly increasing to about 700 m a.s.l. all around except towards the Southern sectors, where the plain elongates. It covers an area of about 24 km^2. Ground coverage includes mainly cultivated terrains, urban areas, roads, and riparian vegetation. Based on these characteristics, this site is convenient as a sample area for surface spectral measurements and subsequent surface reflectance calculations.

The campaign was accomplished on the 10 November 2014 at 12:00 local time (11:00 UTC). The flight plan included six overlapping flight lines aligned approximately NW-SE along-track, about 30° off the solar principal plane (Figure 1). The scheduled 20% along-track overlap was overall matched and often increased, except for adjacent flight lines T2

and T3, where only a few percent overlap has been accomplished. The consecutive flight lines had opposite headings, thus allowing acquiring data in forward and backscattering modes, according to the Sun position.

Geometric accuracy

Orthorectification is the process of transformation from a central projection of the original image to a parallel projection. Displacements due to the tilt of the sensor and to the terrain relief have to be accounted for and corrected (Aguilar, Aguilar, Agüera, & Sánchez, 2007).

We accomplished the georeferencing and orthorectification of our dataset via the manufacturer-provided software. Since the morphology of the overflown surfaces spans from flat to gently hilly terrains, we also used, as input data, a medium resolution DEM with a grid spacing of 10 m. The DEM was obtained from digitised contour lines extracted from the 1:5000 Regional Technical Maps series (C.T. R.) and then interpolated.

We evaluated the geometric accuracy of the orthorectification process through co-registration of a number of Ground Control Points (GCPs) to the cartographic orthophotos acquired in 2013. We accomplished the statistical analysis of the displacements of a number of GCPs and with respect to an independent and high quality dataset. This evaluation allowed us to understand the geometric quality of our dataset and the effectiveness of processing using the DaedalusScanners proprietary tool.

Field survey

Field survey was carried out simultaneously to the overflight, in order to retrieve accurate surface reflectance factors. We collected *in situ* spectra using a portable ASD (Analytical Spectral Devices Inc., Boulder, CO, USA) field spectrometer FieldSpec PRO. The instrument measures light intensity in the range between 350 and 2500 nm using the standard bare fibre-optic cable that collects the reflected radiation within a 25°conical FOV.

Target sites have been accurately selected in order to ensure both the statistical representativeness of the *in-situ* measurements for data calibration purposes (which is strongly dependent on time constrains and, in turn, requires that the selected targets are easily accessible, measurable, and distributed within a relatively small area), and proper characterisation of the dynamic range of radiance within the study area. Therefore, we carefully verified the adequacy of target sites to the following criteria: (a) high spatial homogeneity, compared with the spatial resolution of the imagery dataset; in the ideal case, each target covers

Figure 1. Context and location of the Peligna Valley test site (Abruzzo, Italy). The inset shows the footprints of the 6 flight lines accomplished, and ground position of the targets of the spectroradiometric field survey (red circles). Each flight line has been named from T1 to T6 and the Sun position at the starting time of the measurements, has also been represented. The base maps are the Bing Mapping APIs (main image) and the 2013 orthophotos of the Abruzzo Region of Italy, in the inset.

an area of approximately 5 × 5 squared pixels in the reference imagery; (b) representativeness of the dynamic range of radiance in the region; (c) low adjacency effects (targets located at adequate distance from other volumetric scattering disturbances); (d) low slope effects (targets with flat surfaces); (e) low temporal variability of the spectral response (targets with stable spectral response, not displaying rapid changes due to short-term dynamics phenomena). Although not easy to accomplish in the field, all these requirements contribute to strongly reduce the distortion effects arousing from the use of *in-situ* measurements in remote sensing applications. Following a preliminary identification in Google Earth®, eight sites were visited in the field and deemed suitable for data collection. This made planning and execution of a coherent sampling strategy which allowed a number of 18 targets to be acquired. The measured surface types included bare soils, sparse vegetation, cultivated fields, asphalts and concrete (Table 3). Measurements were acquired between 10:00 and 13:00 h local time under conditions of scattered cumulus cloud alternating to clear sky. To limit this source of error, we prudently avoided data acquisition during cloud overpass and carefully registered the cloud cover as a percentage of the hemisphere, to assist the subsequent post-processing. The cross-check between measurements of reference panel and target material allowed each measurement to be validated.

Eleven calibration targets were used, and for accuracy assessment purposes a further seven validation targets were identified (Table 3).

Each target was measured by averaging 10 spectra of radiance values. To obtain reflectance data, we used a Labsphere Spectralon® (Labsphere Inc., North Sutton, NH, USA) white reference panel and acquired the white reference before the measurement of each target. Spectral measurements were acquired from

1.5 m height, giving about 65 cm Ground Instantaneous Field Of View at nadir. All the spectra were averaged to yield a single mean corrected reflectance spectrum for each target, which was then convolved to the band centres of the airborne CZCS sensor. The standard deviation of the means so far calculated is within 3.7×10^{-6} and 8.5×10^{-3} units of radiance (Watts/meter^2/nanometer/steradian).

Selection of appropriate cal/val targets

According to Smith and Milton (1999), the selection of calibration targets is a critical aspect in the vicarious calibration method based on the empirical line (EL) assumption. Therefore, the field targets used for EL correction should have the following characteristics: cover an area several times the pixel size of the sensor and be at an elevation similar to the areas of interest in the image; be near Lambertian, and devoid of vegetation or other temporary variant features, and maintain a wide dynamic radiometric range encompassing the range of brightness values on the mission (Smith & Milton, 1999; Baugh and Groeneveld, 2008; Brook & Ben-Dor, 2011; Staben, Pfitzner, Bartolo, & Lucieer, 2012; and references therein).

The concept of target stability in space and time is particularly appropriate when vicarious calibration *s. s.* is applied to multi-temporal datasets (Brook & Ben-Dor, 2011; Clark et al., 2011b). In our case, ground calibration targets have not to be considered as pseudo-invariant in time and space because their employment is limited to the present dataset and the field survey is concomitant with the overflight. According to Secker, Staenz, Gauthier, and Budkewitsch (2001), the calibration has the additional advantage of being performed with data acquired at the time of sensor overpass.

Vegetated terrains show large coefficient of variations (COVs) when spatially distributed measurements are acquired with similar illumination and reflection geometries (Karpouzli & Malthus, 2003). Therefore, we reasonably could accept vegetated surfaces as calibration targets as long as the cover type and distribution is homogeneous within the selected target. We understand that vegetated terrains have non-Lambertian reflectance behaviour. Nevertheless, real surfaces display non-Lambertian reflectance behaviour to some extent (Clark et al., 2011b; Pinter, Jackson, & Moran, 1990; Smith & Milton, 1999).

The requirement of near Lambertian target surface deserves further consideration. We did not account for the BRDF (Bidirectional Reflection Distribution Function) of the selected targets during the field survey. We collected observations from nadir-pointed radiometer in the field, while the airborne CZCS sensor acquired upwelling radiance coming from the

Table 3. Ground targets measured during the field survey at the Peligna Valley.

Site	Target	Longitude	Latitude	Purpose	Surface type
ST1	S1	13.841	42.135	VAL	Bare soil
ST1	S2	13.840	42.135	CAL	Asphalt
ST1	S3	13.840	42.135	CAL	Grass
ST2	S1	13.842	42.135	CAL	Vineyard
ST2	S2	13.842	42.135	VAL	Bare soil
ST3	S1	13.836	42.119	VAL	Asphalt
ST3	S2	13.836	42.118	VAL	Paving
ST3	S3	13.836	42.118	CAL	Dry leaves
ST4	S1	13.835	42.117	CAL	Corn field
ST4	S2	13.835	42.117	VAL	Concrete
ST4	S3	13.835	42.117	CAL	Asphalt
ST5	S1	13.827	42.111	CAL	Grass
ST5	S2	13.827	42.110	CAL	Concrete
ST6	S1	13.834	42.116	VAL	Reddish bricks
ST6	S2	13.834	42.116	CAL	Grass
ST7	S1	13.856	42.113	CAL	Bare soil
ST8	S1	13.858	42.113	CAL	Bare soil
ST8	S2	13.859	42.113	VAL	Dry grass

surface within 86° FOV. It means that the sensor is ±42° off-nadir viewing angle range. Therefore, the assumption of near Lambertian target surfaces cannot be verified. As a consequence, we expect an amount of deviation from collinearity between ground-based and at-sensor radiance as a function of the off-nadir viewing angles (Pinter et al., 1990).

In this study a total of 18 targets were measured in the field. Eleven selected ground targets were used to derive the prediction equation between the at-sensor radiance and surface reflectance for each waveband, while the remaining seven were used to assess the accuracy of the prediction equations (Table 3). The location of each target was recorded using an handled GPS with accuracy of ±3 m. The distribution of the field targets span the whole area covered by the remote observations and the elevation ranges between 360 and 260 m a.s.l. in 3.5 km cross-track length. Each flight line includes two targets at least. Image T3 has no targets within (Figure 1).

The empirical line method

A widely used and potentially very accurate technique of achieving absolute atmospheric correction is the calibration of raw DNs or at-sensor radiance (L_{SS}) to surface reflectance factor (ρ_s), assuming a linear relationship between them (Equation 1) (Roberts, Smith, & Adams, 1993; Smith & Milton, 1999; Karpouzli & Malthus, 2003; Baugh and Groeneveld, 2008; Clark et al., 2011a, 2011b; and references therein). The goal is to retrieve ρ_s which is defined as the ratio of the radiant flux reflected by a surface to that reflected by an ideal Lambertian standard surface under identical conditions of illumination, reflection geometry and wavelength interval. Farrand et al. (1994) used the definition of "apparent reflectance" to qualify ρ_s and thus account for the illumination and reflection geometry of a given pixel. In spectral field surveys, it is possible to measure the ρ_s by approximating the Lambertian standard surface with a Spectralon® panel. EL methods can then be used to estimate ρ_s from remotely sensed data, using the following equation:

$$\rho_s(\lambda) = A_{ch} \cdot L_{SS} + B_{ch} \quad (1)$$

where A_{ch} is the multiplicative term which affects the radiance, primarily due to atmospheric attenuation; and B_{ch} is the additive term mainly due to atmospheric path radiance. Both the coefficients can be determined using a least squares fitting approach.

The main assumptions obviously are that the atmosphere is almost equally contributing to the radiance reflected throughout the image area and the relationship between ρ_s and L_{SS} is linear. According to Staben et al. (2012), the relationship between radiance and reflectance across the whole data range is quadratic. Nevertheless, Staben et al. (2012) agree that in the range 0–70% the at-sensor radiance and ground reflectance have essentially a linear dependency. Some authors use the linear relationship between at-sensor reflectance and surface reflectance factors to atmospherically correct or validate surface reflectance factors retrieved from remote sensing measurements (Jun-Feng & Jing-Feng, 2008; Liu et al., 2010; Moran et al., 2001).

Despite widely and successfully used, the EL correction can easily introduce artefacts to the corrected data and should thus be used with caution (Brook & Ben-Dor, 2011). EL approaches are complicated by the off-nadir viewing sensor capability, as it is the case of the CZCS scanner. In such conditions, the sensor IFOV increases as a function of the distance from nadir and the viewing geometry changes accordingly. As a consequence, the upward radiance collected by the sensor comes from surfaces of different areas in the cross-track direction, and the BRDF should be accounted for, in order to retrieve accurate surface reflectance factors. However, while the former effect is partially compensated via the geometric corrections applied to the dataset in the pre-processing stage, it is acknowledged that in the majority of the field surveys, including the present one, it may only be possible to collect nadir reflectance measurements (Clark et al., 2011a). Further errors may be introduced due to changes in the atmospheric path length as a result of elevation differences between calibration targets and regions within the imagery (Staben et al., 2012). As a result, a certain amount of error in the estimates of the surface reflectance factors with the ELM have to be expected and cannot be completely removed.

Accuracy assessment

Since direct georeferencing without ground control relies on the extrapolation process only, remaining errors in the system calibration will significantly decrease the accuracy of object point determination (Cramer & Stallmann, 2002). According to Aguilar et al. (2007), a reliable geometric accuracy can be expressed as the sum of independent errors in the sensor orientation phase and in the DEM extraction, when a DEM is required for the processing. Mathematically, both the variance of the residuals after sensor orientation using the geometric correction model and the planimetric accuracy of the DEM affect the overall variance of the residuals in the orthorectified image.

The Root Mean Square Error (RMSE) is a widely used and accepted statistical metric to measure model performances. Many authors used RMSE to illustrate the error distribution of the geometric correction model by using GCPs identified in independently

derived orthophotos (Aguilar et al., 2007; Mei, Bassani, Fortinovo, Salvatori, & Allegrini, 2016). The underlying assumption when presenting the RMSE is that the errors are unbiased and follow a normal distribution (Chai & Draxler, 2014).

However, Willmott, Matsuura, and Robeson (2009) demonstrated that sums-of-squares-based error statistics, such as RMSE, are inappropriate measures of the average or typical error because they suffer from inherent ambiguities. The authors instead recommend to use the mean-absolute error (MAE) as a natural and unambiguous measure of the average of the error magnitudes.

Besides the critical opinions of the best ways to account for model errors, which are beyond the purpose of the present investigation, our main interest was to correctly provide an evaluation of the residual distributions after matching either ground reference points or GCPs derived from a different dataset, to their counterparts in our dataset. Therefore, we used the RMSE, and MAE to account for the geometric error still remaining after sensor self-calibration (equations below).

$$RMSE = \sqrt{\frac{1}{n}\sum_{n}^{i=1} e_i^2} \qquad (2)$$

$$MAE = \frac{1}{n}\sum_{i=1}^{n}|e_i| \qquad (3)$$

where n is the number of errors or residuals e.

We apply both the equations to the orthorectified data acquired during the campaign over the Peligna Valley, by measuring the displacement of selected GCPs with respect to regional of 2013.

The accuracy assessment of the EL correction followed analogue criteria. In addition to the previous metrics, we also used some measures of so called goodness-of-fit, such as the coefficient of determination (R^2) and the adjusted coefficient of determination (R^2_{adj}), according to numerous examples existing in the current literature (e.g. Baugh and Groeneveld, 2008; Karpouzli & Malthus, 2003; Mei et al., 2016; Vaudour, Moeys, Gilliot, & Coquet, 2008).

Results and discussion

Geometric correction

Figure 2 shows, on top, the whole dataset acquired over the Peligna Valley. All the images are in units of radiance ($\mu W \cdot cm^2 \cdot nm \cdot sr$) and projected according to the UTM grid system, as a result of the pre-processing via the manufacturer-provided software. Accuracy assessment of the orthorectification process has been evaluated through the statistical analysis of the displacements of a number of GCPs co-registered
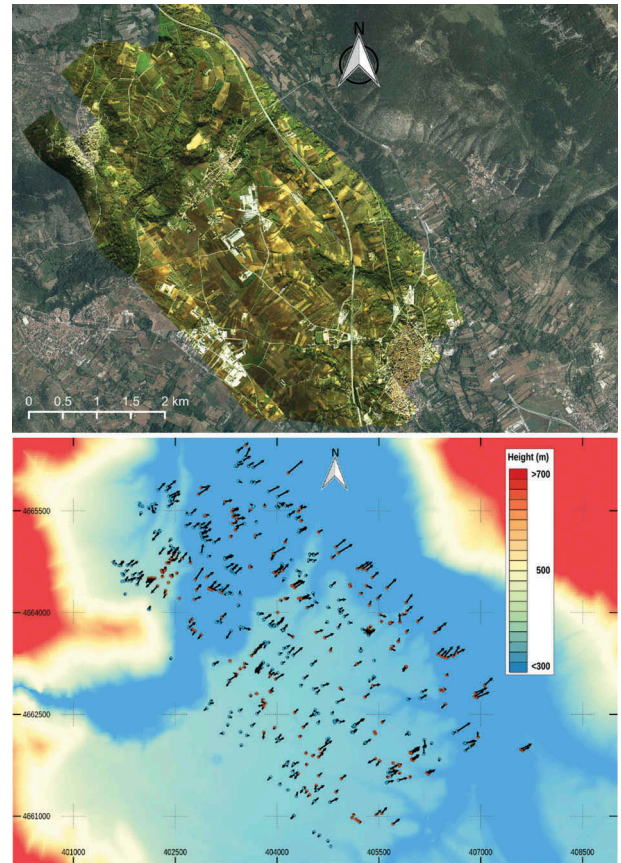
Figure 2. (top) Dataset acquired during the Peligna Valley Campaign. The images are in units of radiance ($\mu W \cdot cm^2 \cdot nm \cdot sr$) and projected in the UTM grid system. The dataset has been directly georeferenced and orthorectified through the manufacturer-provided software tool. The base map is a mosaic of orthophotographs acquired in 2013 on behalf of the Cartographic Service of Abruzzo Government. (bottom) Spatial distribution of the GCPs displacements, as revealed during the co-registration with the 2013 orthophotographs. The base map is the 10 m ground resolution DEM provided by the Cartographic Service of Abruzzo Government.

with the 20 cm spatial resolution orthophoto. Figure 2 (bottom) shows the spatial distribution of the GCPs displacements, with 20 times magnitude exaggeration.

The displacements have been statistically analysed according to the X (longitude) and Y (latitude) components and the results are shown in Figure 3 and listed in Table 4. In few cases they approximate the normal distribution but more often the data show marked non-normal distributions. Average and median values are always positive, thus implying that after pre-processing, the images are narrower than the orthophotos of the same area, used as references. Therefore, the main part of the GCPs will move towards the North and East directions after co-registration with orthophotos (Figure 2).

Figure 2 also shows higher magnitude displacements located along the easternmost borders of the images. Also Table 4 lists the highest displacements

Table 4. Geometric accuracy of the remote sensing dataset.

Flight line	GCPs	MAE (m)			RMSE (m)		
		X	Y	2D	X	Y	2D
T1	80	3.21	2.67	4.17	4.07	3.39	5.30
T2	83	3.06	2.22	3.78	3.77	2.73	4.65
T3	70	3.68	1.84	4.12	4.38	2.30	4.95
T4	139	3.22	2.57	4.12	3.76	3.10	4.88
T5	95	2.38	2.54	3.48	3.02	3.15	4.37
T6	59	2.18	1.88	2.88	2.70	2.27	3.53

Flight line	GCPs	Mean error (m)		Median error (m)		Maximum error (m)	
		X	Y	X	Y	X	Y
T1	80	2.45	1.72	1.77	1.78	10.65	9.16
T2	83	2.14	0.57	2.35	0.74	9.62	7.25
T3	70	2.99	1.27	3.38	1.16	8.76	4.96
T4	139	1.83	0.58	2.11	0.96	8.23	6.70
T5	95	0.76	0.64	0.23	0.54	8.88	8.74
T6	59	1.73	1.26	1.48	1.38	6.45	6.46

along the longitude direction (X). Since the flight-lines have opposite headings while scanning the area from East to West, this behaviour is probably independent on some attitude deflection of the aircraft. It is most probably dependent on the topography of the overflown terrains which is slowly degrading in elevation from West to East (about 100 m in 3.5 km distance), and the algorithm used for geometric correction, as well. Unfortunately, we do not know the algorithm implemented within the blind-box software for pre-processing CZCS data.

The quality of the DEM resolution has certainly its role in the general accuracy of the orthorectification process, as demonstrated by Aguilar et al. (2007). The authors suggested that, when measured independently, the error of the orthoimage is the sum of the error in the sensor orientation phase plus the error due to the DEM. Since we ignore the DEM accuracy, our estimate of the total accuracy in the orthorectification process is empirically calculated through secondary non-parametric geometric correction with orthophotos available for the same area. An additional source of errors when secondary geometric correction is applied, is due to arbitrary displacements introduced in the positioning of GCPs on the imagery. Unfortunately, this error is random and not easily estimated. However, it has the magnitude of the smaller pixel (20 cm in the orthophotos), at least.

As shown in Table 4, the bi-dimensional MAE is always lower than the RMSE, as expected (Chai & Draxler, 2014) and varies between 2.88 and 4.17 m, that corresponds to approximately one to two image pixels, at the given resolution. Maximum displacements are in the range between 4.96 and 10.65 m, although they are very isolated values and are possibly influenced by random inaccuracy in pixel pointing. As a consequence, since the MAE gives the same weighting to all the error magnitudes (Chai & Draxler, 2014), while in the RMSE calculation, the highest magnitudes of individual errors strongly

influence the results, we are favourable to the use of the MAE as a measurement of geometric accuracy.

Since the error distributions are not strictly Gaussian (Figure 3), the average error and RMSE appear as little appropriate to correctly describe the geometric accuracy, because the assumption underling both these metrics is that there is no deviation from normality in the dataset. In addition, the sign of the geometric displacements are conventionally attributed according to the direction of the displacement itself. This peculiar property of spatial displacements around reference GCPs makes the MAE as more favourable than the mean for the measurement of the average error magnitude.

As a result, by using secondary geometric correction of airborne imagery with GCPs, we assess the geometric accuracy of our dataset through only evaluating the errors due to the displacements of GCPs with respect to orthophotos and thus assuming both the DEM and orthophotos not contributing as additional sources of errors. With these premises, the geometric accuracy of the aerial imagery is acceptable for applications such as geological and/or archaeological surveys over hilly terrains. It is worth noting that having the chance of using higher resolution DEMs of the same area will certainly improve the geometric accuracy of the dataset to values more than acceptable.

EL correction

Figure 4 shows the whole spectral measurements acquired during the field survey at the Peligna Valley, and resampled according to the CZCS spectral bandpasses. Resampling has been carried out by convolving the ASD-FieldSpec ground spectral measurements with the CZCS filter functions. Spectral resampling is required in order to calculate linear regression functions at each wavelength of interest. In Figure 4, spectra are presented in four separate panels, according to their overall albedo and general shape.

Asphalts (top left panel) show featureless spectra with a wide variability in overall albedo, probably according to weathering and ageing processes (Clark et al., 2011b; Herold & Roberts, 2005). Through observing the spectral behaviour of a number of asphalt-made surfaces having a range of ages and distresses, Herold and Roberts (2005) were able to establish a relationship between degree of maturity and overall albedo. The younger the age, the lower is the overall reflectance of the asphalt. The typical features in the SWIR region, due to hydrocarbon and mineral constituents cannot be resolved at the CZCS bandwidths.

Bare soils (bottom left panel) have the lowest overall albedo in the whole dataset. Bare soils have high
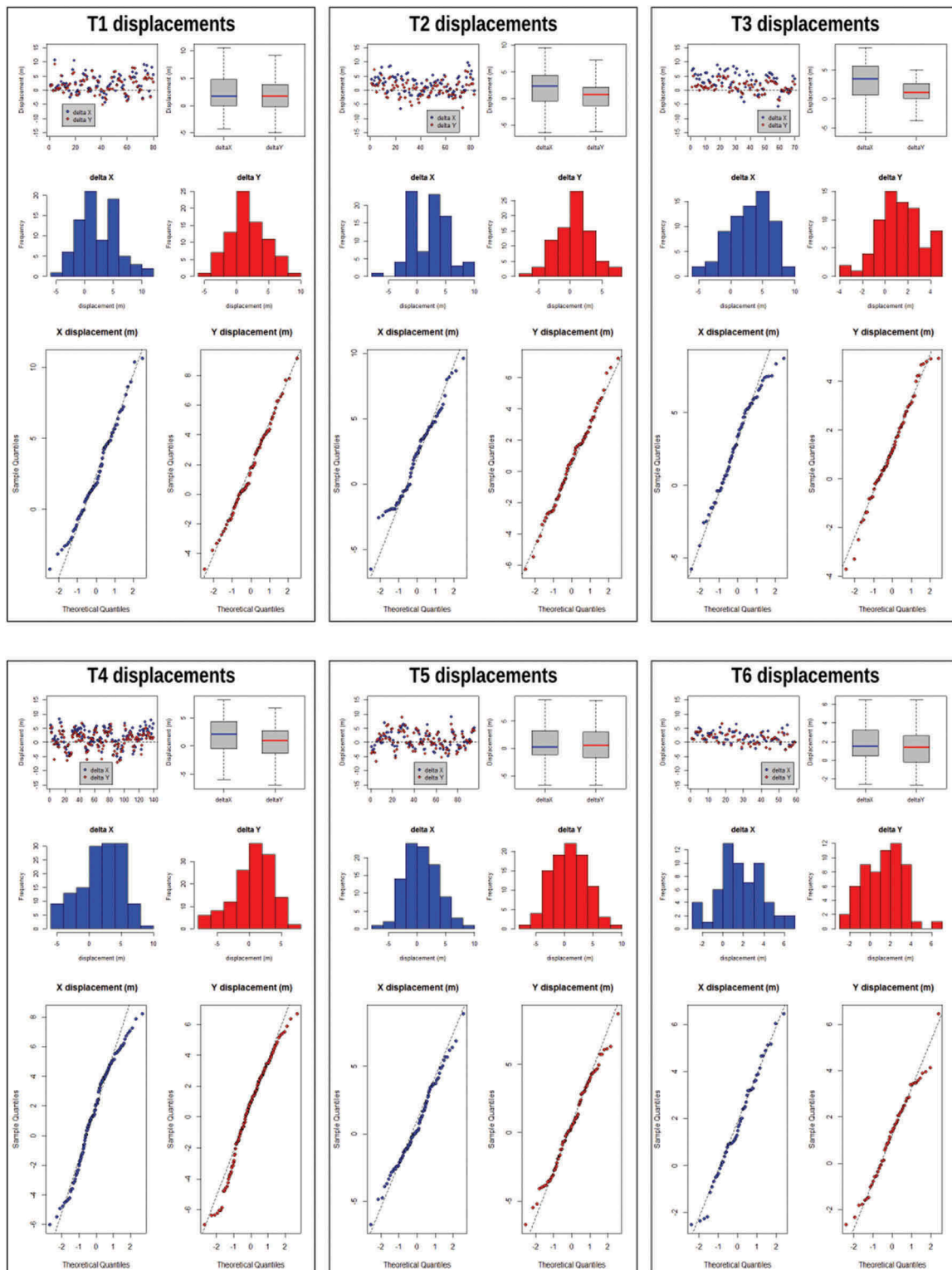
Figure 3. Descriptive statistical diagrams of the X (longitude) and Y (latitude) displacements measured for each set of corresponding GCPs used in the co-registration process with orthophotographs. From top: index plot, box-and-whisker plot, frequency plot and q-q plot.

degrees of roughness at their surfaces and this is possibly responsible for the low overall albedo, allowing the presence of light sinks and shadows due to the very irregular surfaces. They show a weak absorption feature near 0.7 μm and therefore are distinguishable from the youngest asphalt. They also show less steep spectra in the visible region than asphalts. The whole set of measured bare soils shows low variance at all the wavelengths.

The top right panel in Figure 4 shows the reflectance spectra of vegetated terrains with diagnostic features in the VIS and NIR spectral regions. The prominent red edge peak varies according to the type and healthiness of vegetation. Man-made
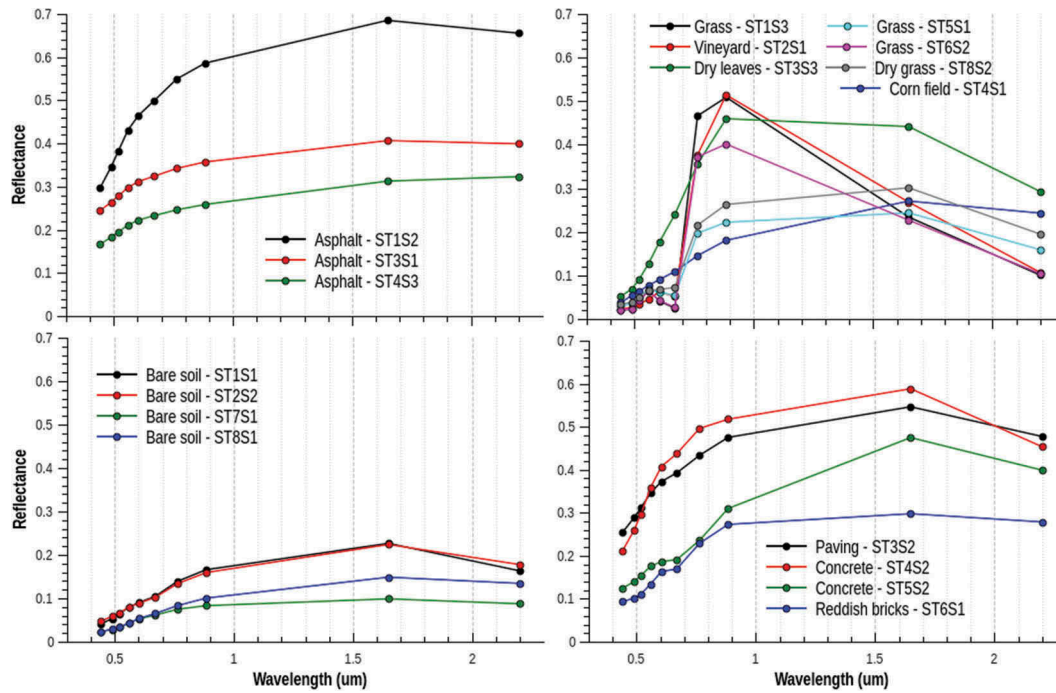
Figure 4. Ground target spectra resampled according to the CZCS filter functions.

surfaces (bottom right panel) display diagnostic features in the visible to near-infrared wavelength regions and a wide variability of overall spectral shape and albedo.

Although frequently used to establish pseudo-invariant targets for use in EL calibration (Clark et al., 2011b; Jun-Feng & Jing-Feng, 2008; Karpouzli & Malthus, 2003), the COV has not been evaluated in the present investigation. Here we carried out a point sampling strategy during the survey, in order to accomplish the main part of the measurements contemporary to the sensor overpass. Although we did not assess the spectral variability of each single target surface, our ground-based measurements are indeed useful for EL calibration as long as the targets have sufficiently wide extension compared to the pixel resolution and near Lambertian behaviour with respect to the incident light. Obviously this last property is not common to be observed in nature and is responsible for great part of the uncertainty in EL calibrations. The ground target spectra used with the ELM were obtained by averaging 10 consecutive measurements, virtually acquired on the same point.

For ELM application, Ground Calibration Targets and Ground Validation Targets are selected in order to cover the whole reflectance dynamic range (bright and dark targets). Radiance values are extracted from imagery by averaging four pixels of 1.5 m around the corresponding target positions (Karpouzli & Malthus, 2003). These values are plotted against the corresponding ground reflectance and linear regression applied to obtain prediction equations for each CZCS band. Regression proceeds by minimising the errors in the response variable (y, the ground

reflectance), for a given value of the predictor variable (x, the at-sensor radiance). This gives the minimum variance unbiased predictor of y for a given x. Standard errors of the estimated parameters, coefficients of determination and adjusted R-squared are also provided (Figure 5 and Table 5). Figure 5 also shows the 95% confidence intervals of the fitted values.

In general, the calibration equations estimated for each sensor waveband have lower coefficients of determination in the SWIR spectral region than the VIS (Table 5). Since the R-squared is the fraction of the total variance explained by the model, the higher dispersion of the fitted data in the SWIR region than the VIS accounts for this behaviour. The adjusted R-squared differs from R-squared in that it is based on the overall variance and the error variance. Therefore, adjusted R-squared provides an adjustment to the R-squared statistic because each independent variable (x) that has a correlation to the dependent variable (y) increases adjusted R-squared and vice versa. This is a very desired property of a goodness-of-fit statistic. Nevertheless, in our case, the calibration lines in the SWIR region are still less precise than in the VIS region, as already observed (Mei et al., 2016).

Confidence intervals associated with predictions (Figure 5) deal with the uncertainty about the predicted reflectance values. Uncertainty increases with the square of the difference between the mean value of x and the value of x at which the dependent variable (y) is to be predicted. This behaviour is clearly shown in Figure 5 where the main uncertainties are generally observable towards higher radiance

values. The ground calibration targets we used in the present study show overall low albedo at all the wavelengths and thus the points in Figure 5 mainly cluster in the lower margin of the plots. As a result, the mean value of the independent variable (the at-sensor radiance) shifts to the low radiance region at all the wavelengths and, in turn, the distance between this low mean radiance and the isolated points with the highest radiance increases, thus enlarging the confidence limits.

Standard errors of the estimated slope and intercept measure the uncertainty associated with the estimated parameters of the model. They both increase with increasing variance and decrease with increasing number of points to be fitted. Intercept always shows higher uncertainty than the slope (Table 5) and in several cases the uncertainty is comparable with the estimated values, as order of magnitude. The uncertainty of the slope estimates is always considerably low. However, the uncertainty of the intercept and slope estimations are always lower than and comparable to the values obtained by Hamm, Atkinson, and Milton (2012), respectively.

Seven ground validation targets have been selected as to include a wide range of surface covers (Table 3) and be distributed within a number of images. Figure 6 shows the distribution of the residuals between the measured and estimated reflectance after applying the
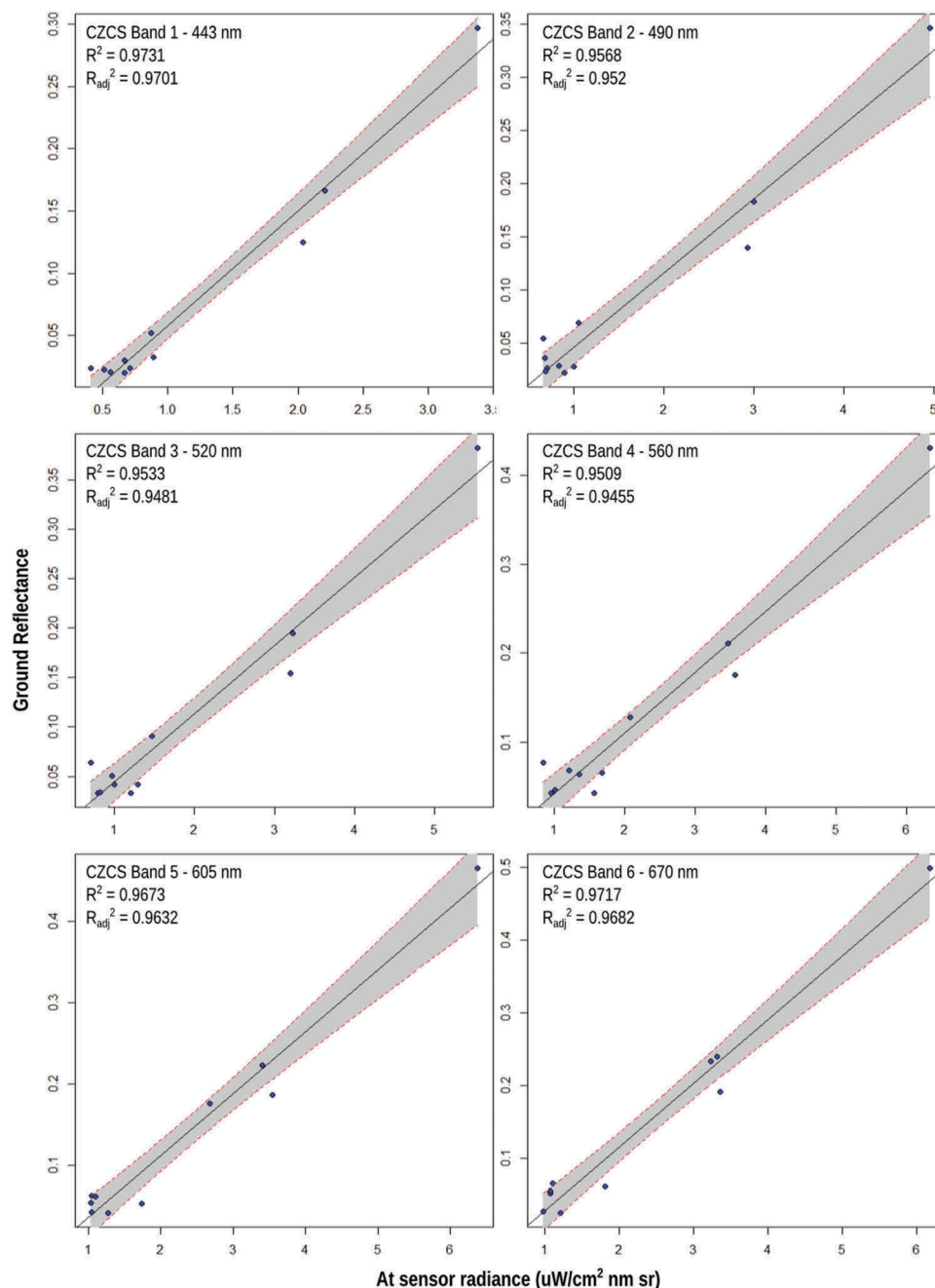
Figure 5. Scatterplots and least squares regressions for ground reflectance (portable ASD-Fieldspec spectroradiometer) against at-sensor radiance (airborne CZCS). Red dashed lines represent the upper and lower 95% confidence limits of the fitted values. Coefficients of goodness-of-fit are also reported. See the text for explanation.
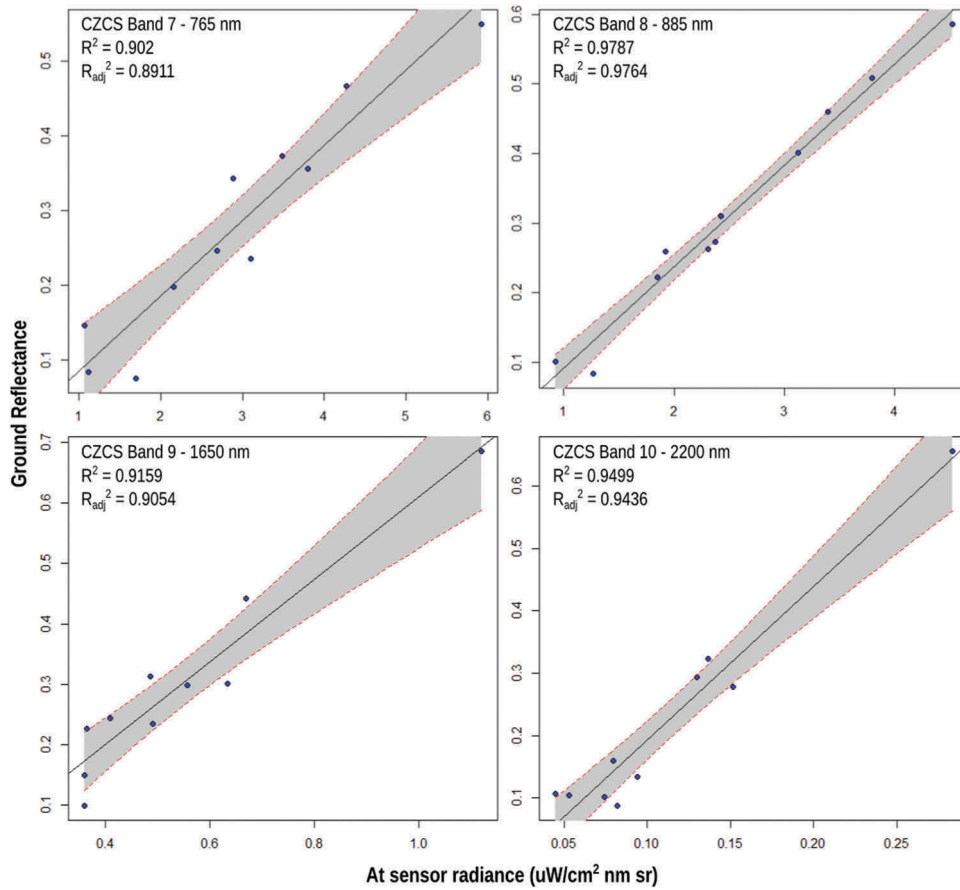
Figure 5. (Continued).

Table 5. Results of the ELM.

	Band 1	Band 2	Band 3	Band 4	Band 5	Band 6	Band 7	Band 8	Band 9	Band 10
Intercept	−0.0340	−0.0235	−0.0250	−0.0264	−0.0401	−0.0596	−0.0158	−0.0548	−0.0740	−0.0530
St.er.	0.0076	0.0103	0.0119	0.0140	0.0141	0.0150	0.0358	0.0196	0.0431	0.0261
Slope	0.0921	0.0698	0.0690	0.0682	0.0761	0.0875	0.1007	0.1457	0.6845	2.4594
St.er.	0.0051	0.0049	0.0051	0.0052	0.0049	0.0053	0.0111	0.0072	0.0733	0.1998
R2	0.9731	0.9568	0.9533	0.9509	0.9673	0.9717	0.9020	0.9787	0.9159	0.9499
R2adj	0.9701	0.9520	0.9481	0.9455	0.9632	0.9682	0.8911	0.9764	0.9054	0.9436
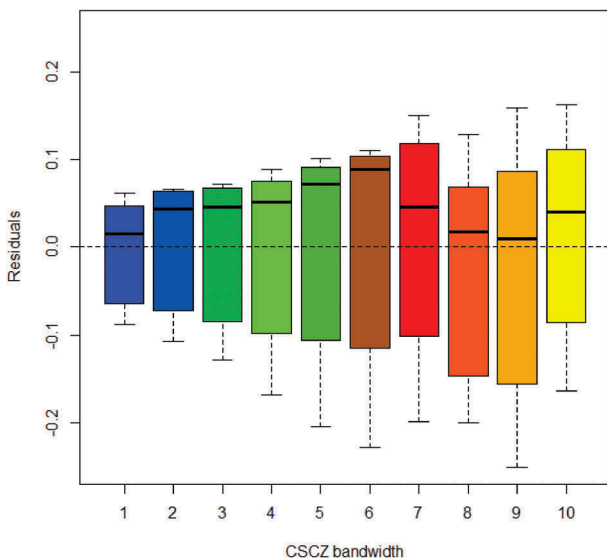
Figure 6. Box-plots of the residual distribution obtained with ground validation targets.

EL calibration, at each CZCS waveband. Residuals of the estimated reflectance of ground validation targets range between ±0.1 reflectance in the visible wavebands and slightly increase in the SWIR region. This behaviour reflects the increasing uncertainty of the model estimates at longer wavelengths. Average values are slightly negative and very close to the 0 mean. Medians are always positive and generally higher than the averages except for CZCS bands 8 and 9. MAE and RMSE of the residuals at each waveband of the validation target spectra (Table 6) are comparable to Mei et al. (2016) and Teillet et al. (2001), who used a larger number of target spectra, but higher than those reported by other authors (Hamm et al., 2012; Karpouzli & Malthus, 2003; Vaudour et al., 2008).

In the majority of our ground validation targets, the reflectance calculated with the EL method is overestimated (Figure 7). Overestimation of the

Table 6. Results of the validation process (the statistics are expressed as units of reflectance).

Waveband (μm)	MAE	RMSE	Mean	Median
0.443	0.0554	0.0593	−0.0066	0.0148
0.490	0.0700	0.0722	−0.0019	0.0431
0.520	0.0786	0.0822	−0.0064	0.0462
0.560	0.0936	0.1000	−0.0104	0.0511
0.605	0.1100	0.1175	−0.0088	0.0714
0.670	0.1235	0.1315	−0.0074	0.0888
0.765	0.1194	0.1290	0.0044	0.0463
0.885	0.1112	0.1304	−0.0299	0.0179
1.650	0.1291	0.1494	−0.0316	0.0091
2.200	0.1086	0.1162	0.0130	0.0402

reflectance in calibrated data occurs in bare soils, reddish bricks paving and dry grass targets. Asphalt and some concrete paving show instead underestimation of the reflectance after calibration with the ELM approach. Apparently, overestimation of reflectance occurs in the lowest overall albedo targets and vice versa. The behaviour is consistent to all the wavelengths and has the effect of only slightly altering band ratios, because variations occur all in the same direction per each spectrum. Band ratios are widely employed in a variety of applications involving indices determinations. Nevertheless, monotonic reflectance variations at all the wavelengths of interest such as the predicted reflectance of dark objects is overestimated while that of bright objects is underestimated, have the effect of generally reducing the spectral contrast in the reflectance space.

For the ELM the main objective is to estimate reflectance, given the radiance acquired from remote sensors. Error or residual variability of the response variable (reflectance) may arise, for example, due to fluctuations in the pointing direction of the instrument, sensor noise, positional uncertainty and spatial–temporal variability (Hamm et al., 2012). Even the opposite viewing geometry in consecutive flight lines affects the calibration of the surface reflectance and is accounted for in the total amount of errors inherent in the model. Since the sources of errors with the ELM application are manifold, the key point in order to use the reflectance calibrated data for quantitative applications, is to preserve at least band ratios and overall spectral shape. Nevertheless, the ELM approach can be further improved by accomplishing rigorous field surveys and selecting the ground targets properly.

As with many other atmospheric correction techniques, the ELM assumes that the atmospheric properties are uniform across the image. This is often incorrect and, in particular, water vapour can vary over short temporal and spatial scales. Variations attributed to the light path length or to some inhomogeneities in the water vapour abundance (Farrand et al., 1994) can also occur when ground targets are sampled at different heights. In most situations, insufficient data are available to describe the atmospheric variability. In the absence of appropriate data this effect cannot be accounted for, although it can be limited by undertaking an airborne campaign during stable atmospheric conditions.

Conclusion

In this study, we assessed the geometric and radiometric accuracy of the CZCS sensor on-board the Italian Coast Guard aircraft. To this aim, we
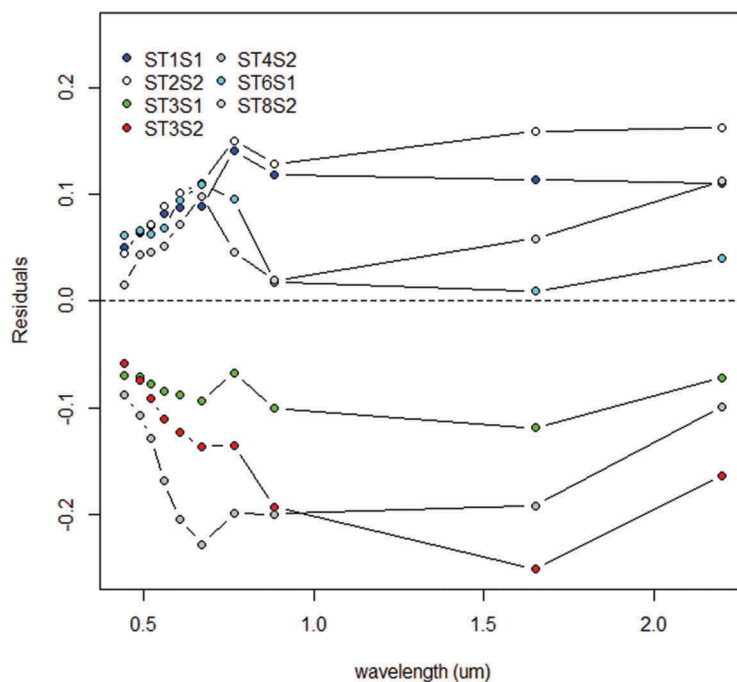
Figure 7. Plot of the residuals between actual and estimated reflectance of ground validation targets, at each CZCS waveband of interest.

attempted to provide an estimate of both the geometric uncertainties of CZCS imagery when the remote sensing campaign is accomplished on hilly terrains, and the uncertainties associated with the atmospheric correction using the ELM.

By applying secondary non-parametric geometric correction with 20 cm spatial resolution orthophotos available for the same area, we were able to assess the mean absolute error corresponding to approximately one to two image pixels, at the given resolution. We accomplished this result through only evaluating the errors due to the displacements of GCPs with respect to orthophotos and thus assuming both the DEM and orthophotos not contributing as additional sources of errors. With these premises, the geometric accuracy of the aerial imagery is acceptable for quantitative applications.

The ELM is a simple and valuable method for the spatial retrieval of surface reflectance from remote sensing imagery. The correction dataset must be carefully selected to cover the whole range of reflectances, to be of an appropriate size in respect to the pixel size of the imagery and have as much as possible near-Lambertian properties, so as to exclude outliers and minimise residual errors. The method relies on the availability of ground data measurements contemporary to the sensor overpass and under clear sky conditions.

Although the validation and calibration targets used in this study were similar in nature, the large correlation coefficients observed between at-sensor radiance and ground reflectance for the 10 CZCS wavebands and the independent error assessment demonstrates that the ELM can be applied to correct CZCS imagery with satisfactory results. The high spatial resolution which is possible to accomplish with airborne sensor allowed to identify a large number of natural targets that were sufficiently homogeneous and larger than the pixel size. Targets height differences of about 100 m in the cross-track direction may have some effects on the ground reflectance determination, especially when the flight altitude is only 700 m a.g.l., as is our case, due to differences in the optical paths.

Nevertheless, the possible sources of errors when the EL approach is used for atmospheric correction are manifold, including some inaccuracies in locating the targets on the image. The results reported here are very encouraging and suggest that the errors can be reduced further when using a greater number of calibration targets.

Acknowledgements

Disclosure statement

ORCID

Loredana Pompilio http://orcid.org/0000-0003-3217-7575

References

Aguilar, M.A., Aguilar, F.J., Agüera, F., & Sánchez, J.A. (2007). Geometric accuracy assessment of QuickBird basic imagery using different operational approaches. *Photogrammetric Engineering & Remote Sensing*, 73(12), 1321–1332. doi:10.14358/PERS.73.12.1321

Baugh, W.M., & Groeneveld, D.P. (2008). Empirical proof of the empirical line. *International Journal of Remote Sensing*, 29(3), 665–672. doi:10.1080/01431160701352162

Ben-Dor, E., Kindel, B., & Goetz, A.F.H. (2004). Quality assessment of several methods to recover surface reflectance using synthetic imaging spectroscpy data. *Remote Sensing Environment*, 90, 389–404. doi:10.1016/j.rse.2004.01.014

Brook, A., & Ben-Dor, E. (2011). Supervised vicarious calibration (SVC) of hyperspectral remote sensing data. *Remote Sensing Environment*, 115, 1543–1555. doi:10.1016/j.rse.2011.02.013

Chai, T., & Draxler, R.R. (2014). Root mean square error (RMSE) or mean absolute error (MAE)? - Arguments against avoiding RMSE in the literature. *Geoscience Model Developments*, 7, 1247–1250. doi:10.5194/gmd-7-1247-2014

Challis, K., Kincey, M., & Howard, A.J. (2009). Airborne remote sensing of valley floor geoarchaeology using Daedalus ATM and CASI. *Archaeological Prospection*, 16, 17–33. doi:10.1002/arp.v16:1

Clark, B., Suomalainen, J., & Pellikka, P. (2011a). An historical empirical line method for the retrieval of surface reflectance factor from multi-temporal SPOT HRV, HRVIR and HRG multispectral satellite imagey. *International Journal of Applied Earth Observation and Geoinformation*, 13, 292–307. doi:10.1016/j.jag.2010.12.004

Clark, B., Suomalainen, J., & Pellikka, P. (2011b). The selection of appropriate spectrally bright pseudo-

invariant ground targets for use in empirical line calibration of SPOT satellite imagery. *ISPRS Journal of Photogrammetry and Remote Sensing*, 66, 429–445. doi:10.1016/j.isprsjprs.2011.02.003

Cramer, M., & Stallmann, D. (2002). System calibration for direct georeferencing. *International Archives of Photogrammetry, Remote Sensing and Spatial Information Sciences*, 34(Part 3A), 79–84.

Farrand, W.H., Singer, R.B., & Merényi, E. (1994). Retrieval of apparent surface reflectance from AVIRIS data: A comparison of empirical line, radiative transfer, and spectral mixture methods. *Remote Sensing Environment*, 47, 311–321. doi:10.1016/0034-4257(94)90099-X

Gao, B., Montes, M.J., Davis, C.O., & Goetz, A.F.H. (2009). Atmospheric correction algorithms for hypersectral remote sensing data of land and ocean. *Remote Sensing Environment*, 113, S17–S24. doi:10.1016/j.rse.2007.12.015

Hamm, N.A.S., Atkinson, P.M., & Milton, E.J. (2012). A per-pixel, non-stationary mixed model for empirical line atmospheric correction in remote sensing. *Remote Sensing Environment*, 124, 666–678. doi:10.1016/j.rse.2012.05.033

Herold, M., & Roberts, D. (2005). Spectral characteristics of asphalt road aging and deterioration: Implications for remote-sensing applications. *Applied Optics*, 44(20), 4327–4334. doi:10.1364/AO.44.004327

Honkavaara, E., Ahokas, E., Hyyppä, J., Jaakkola, J., Kaartinen, H., Kuittinen, R., ... Nurminen, K. (2006). Geometric test field calibration of digital photogrammetric sensors. *ISPRS Journal of Photogrammetry and Remote Sensing*, 60, 387–399. doi:10.1016/j.isprsjprs.2006.04.003

Jun-Feng, X., & Jing-Feng, H. (2008). Empirical line method using spectrally stable targets to calibrate IKONOS imagery. *Pedosphere*, 18(1), 124–130. doi:10.1016/S1002-0160(07)60110-6

Karpouzli, E., & Malthus, T. (2003). The empirical line method for the atmospheric correction of IKONOS imagery. *International Journal Remote Sensing*, 24(5), 1143–1150. doi:10.1080/0143116021000026779

Kiema, J.B.K., & Bahr, H.P. (2001). Wavelet compression and the automatic classification of urban environments using high resolution multispectral imagery and laser scanning data. *GeoInformatica*, 5(2), 165–179. doi:10.1023/A:1011442332063

Liu, X., Li, X., Zeng, Q., Mao, J., Chen, Q., & Guan, C. (2010). Validating MODIS surface reflectance based on field spectral measurements. *International Journal Remote Sensing*, 31(6), 1645–1659. doi:10.1080/01431160903474988

Mei, A., Bassani, C., Fortinovo, G., Salvatori, R., & Allegrini, A. (2016). The use of suitable pseudo-invariant targets for MIVIS data calibration by the empirical line method. *ISPRS Journal of Photogrammetry and Remote Sensing*, 114, 102–114. doi:10.1016/j.isprsjprs.2016.01.016

Meinel, G., Netzband, M., Amann, V., Statter, R., & Kritikos, G. (1996). Analysing an ATM-scanner flight over the city of Dresden to identify urban sealing. *International Archives of Photogrammetry and Remote Sensing*, 31(B7), 486–492.

Moniwa, H. (1980). The concept of photo-variant self-calibration and its application in block adjustment with bundles. *XIV Congress of the International Society for photogrammetry*, Hamburg.

Moran, M.S., Bryant, R., Thome, K., Ni, W., Nouvellon, Y., Gonzales-Dugo, M.P., ... Clarke, T.R. (2001). A refined empirical line approach for reflectance factor retrieval from Landsat-5 TM and Landsat-7 ETM+. *Remote Sensing Environment*, 78, 71–82. doi:10.1016/S0034-4257(01)00250-4

Pinter, P.J., Jackson, R.D., & Moran, S. (1990). Bidirectional reflectance factors of agricultural targets: A comparison of ground-, aircraft-, and satellite-based observations. *Remote Sensing Environment*, 32, 215–228. doi:10.1016/0034-4257(90)90019-I

Roberts, D.A., Smith, M.O., & Adams, J.B. (1993). Green vegetation, nonphotosynthetic vegetation and soils in AVIRIS data. *Remote Sensing Environment*, 44, 255–269. doi:10.1016/0034-4257(93)90020-X

Rowlands, A., & Sarris, A. (2007). Detection of exposed and subsurface archaeological remains using multi-sensor remote sensing. *Journal of Archaeological Science*, 34, 795–803. doi:10.1016/j.jas.2006.06.018

Roy, D.P., Devereux, B., Grainger, B., & White, S.J. (1997). Parametric geometric correction of airborne thematic mapper imagery. *International Journal Remote Sensing*, 18(9), 1865–1887. doi:10.1080/014311697217927

Secker, J., Staenz, K., Gauthier, R.P., & Budkewitsch, P. (2001). Vicarious calibration of airborne hyperspectral sensors in operational environments. *Remote Sensing Environment*, 76, 81–92. doi:10.1016/S0034-4257(00)00194-2

Shennan, I., & Donoghue, D.N.M. (1992). Remote sensing in archaeological research. *Proceedings of the British Academy*, 77, 223–232.

Smith, G.M., & Milton, E.J. (1999). The use of the empirical line method to calibrate remotely sensed data to reflectance. *International Journal Remote Sensing*, 20(13), 2653–2662. doi:10.1080/014311699211994

Staben, G.W., Pfitzner, K., Bartolo, R., & Lucieer, A. (2012). Empirical line calibration of WorldView-2 satellite imagery of reflectance data: Using quadratic prediction equations. *Remote Sensing Letters*, 3(6), 521–530. doi:10.1080/01431161.2011.609187

Teillet, P.M., Fedosejevs, G., Gauthier, R.P., O'Neill, N.T., Thome, K.J., Biggar, S.F., ... Meygret, A. (2001). A generalized approach to the vicarious calibration of multiple Earth observation sensors using hyperspectral data. *Remote Sensing Environment*, 77, 304–327. doi:10.1016/S0034-4257(01)00211-5

Vaudour, E., Moeys, J., Gilliot, J.M., & Coquet, Y. (2008). Spatial retrieval of soil reflectance from SPOT multispectral data using the empirical line method. *International Journal Remote Sensing*, 29(19), 5571–5584. doi:10.1080/01431160802060920

Willmott, C.J., Matsuura, K., & Robeson, S.M. (2009). Ambiguities inherent in sums-of-squares-based error statistics. *Atmospheric Environment*, 43, 749–752. doi:10.1016/j.atmosenv.2008.10.005

Zambianchi, E., Calvitti, C., Cecamore, P., D'Amico, F., Ferulano, E., & Lanciano, P. (1990). Marine coastal eutrophication, proceedings of an international conference. In R.A. Vollenweider, R. Marchetti, & R. Viviani Eds., *The mucilage phenomenon in the Northern Adriatic Sea, summer 1989: A study carried out with remote sensing techniques*. Bologna, Italy. 21-24 March, 1990. Elsevier.